Proposal for realizing Majorana fermions without external magnetic field in strongly correlated nanowires

Kaushal K. Kesharpu [1,*] Evgenii A. Kochetov,[1] and Alvaro Ferraz[2]

[1]*Bogoliubov Laboratory of Theoretical Physics, Joint Institute for Nuclear Research, Dubna, Moscow Region 141980, Russia*
[2]*International Institute of Physics—UFRN, Department of Experimental and Theoretical Physics—UFRN, Natal 59078-970, Brazil*

We show that one-dimensional topological superconductivity can be placed in the context of phenomena associated with strongly correlated electron systems. Here we propose a system consisting of a one-dimensional chain of strongly correlated fermions placed on a superconducting (SC) substrate that exhibits a spin-singlet extended *s*-wave pairing. Strong electron correlation is shown to transform an extended *s*-wave SC into a topological SC that hosts Majorana fermions. In contrast to the approaches based on mean-field treatments, no Zeeman or exchange magnetic field is needed to produce such an effect.

DOI: [10.1103/PhysRevB.109.115140](https://doi.org/10.1103/PhysRevB.109.115140)

I. INTRODUCTION

The topological superconductivity with Majorana zero modes (MZMs) is of fundamental scientific importance due to its proposed application in braiding-based quantum computing [1]. The first theoretical proposal for the realization of the one-dimensional (1D) MZM involved placing a 1D quantum wire with spinless electrons on a *p*-wave superconductor [2]. However, from a materials science point of view, this conceptually simple model is hard to realize because a spinless electron does not exist in nature by default, and *p*-wave superconductors are, at best, rare to find. Later several proposals were put forward to eliminate these difficulties by ingeniously combining the proximity-induced *s*-wave superconductivity, the Rashba spin-orbit coupling (RSOC), and the breaking of time reversal (TR) symmetry [3]. In these proposed systems, RSOC was needed for the spin-momentum locking [4], and TR symmetry breaking was needed to create, in effect, the spinless electrons. Using the aforementioned ideas, broadly three types of platforms have been engineered up to now, by placing [5] (i) topological insulators on a superconductor [6,7], (ii) semiconductors with strong spin-orbit coupling on a superconductor [8], or (iii) chains of magnetic atoms on a superconductor [9,10].

In heterostructures, where the topological insulator is placed over the superconductor, the 1D helical edge states provide the needed spin-momentum locking [7]. The 1D edge states occur due to RSOC. The TR symmetry in these heterostructures can be broken, either by applying a magnetic field [11–13], or by either doping with magnetic atoms [14] or placing the magnetic materials in the vicinity of the topological insulators [15,16]. In the case of a semiconductor on superconductor heterostructure, usually a semiconductor wire with strong RSOC and magnetic field are used to satisfy the aforementioned requirements to generate MZMs [8,17]. For

devices with a magnetic adatom chain on a superconductor, the Yu-Shiba-Rusinov (YSR) states induce a spin-polarized subgap in the parent superconductors [9,10]. If the magnetic adatoms are placed very close to each other, the YSR states hybridize, and the hopping between neighboring adatoms broadens the particle-hole symmetric YSR pair states into bands. Once the bands formed by the positive and negative energies overlap at the center of the superconducting gap, the *p*-wave pairing correlations will reopen the gap and turn the adatom chain into a 1D topological superconductor with an MZM. The *p*-wave correlation can be induced either by RSOC in the parent superconductor, or by the helical spin states on the magnetic adatom chain [18].

From the experimental side, claims of MZM in topological insulators (Bi/Nb [19], Bi_2Te_3 [11,20], Bi_2Se_3 [21,22], and $Bi_2Te_{3-x}Se_x$ [14]) have been made. For semiconductors on superconductor platforms, usually InAs and InSb on superconductors have been extensively used in the experiments [8]. Regarding the magnetic adatoms on superconductors, the chain of Fe atoms on Pb [10], Re [23], or Ta [24] substrates has shown signs of the MZM. Despite these experimental successes, several concerns still remain, which have to do mainly with the requirements of the strong RSOC and the external magnetic field. The former limits the candidate materials which can be placed over the superconductor, while the latter limits the possible superconducting substrates. In addition, the crystal symmetry consideration greatly shrinks the possible superconductors supporting topological phases [25]. The external magnetic field is the principal hindrance, because most experiments use *s*-wave superconductors for which their superconductivity might be destroyed in a strong enough magnetic field. Hence, the following question naturally arises: Can we get rid of the constraint imposed by the magnetic field? It is the goal of this article to suggest a different route to realizing the MZM without making use of an external magnetic field.

In a strong magnetic field, the spins of the electrons are aligned along the direction of the applied field. The Pauli constraint prohibits the occupation of more than one fermion

---
*kesharpu@theor.jinr.ru

in a single quantum state. Hence no more than one electron with the same spin can occupy a single site. Physically, it is the same as having spinless fermions. Therefore, one way of realizing the spinless fermions is through the application of a magnetic field. Another way to produce such an effect is to rely on the presence of a large on-site Coulomb repulsion. In such a strong correlation regime, each lattice site becomes at most singly occupied, and the charge and spin degrees of freedom separate from each other. The resulting fermion is effectively spinless, and this is precisely what we need. The prototype model for such a behavior is the $U \to \infty$ Hubbard model [26–28]. The main reason why such an approach was not used before was probably the inadequacy of the mean-field methods to treat strong correlation. In this paper, we show that strong electron correlation can indeed drive the 1D system of lattice electrons into the topological phase as Kitaev's toy model suggests [2]. This consideration is based on the representation of the underlying dynamics in terms of Hubbard operators that encode strong electron correlation effects. The basic requirement of no local double occupancy is taken into account rigorously prior to any mean-field treatments. To this end, the su(2|1) coherent-state action is employed, where the su(2|1) superalgebra incorporates the full set of Hubbard operators [29]. We propose a device in which a strongly correlated nanowire is placed over an extended s-wave superconductor. Usually iron-based superconductors fulfill this requirement [30–32]. The details of experimental realization are discussed in Sec. VII.

It should be mentioned that an analogous idea was presented before [33]. However, instead of a strongly correlated nanowire, a semiconducting nanowire with strong RSOC on an extended s-wave superconductor was proposed in its place. Hence, the problem of using a magnetic field still persisted (although a critical magnetic field of iron-based superconductors is quite high at ∼50 T [34]). In another analogous work, it was predicted that a semiconducting nanowire with C_n ($n > 4$) rotational symmetry and nonzero electronic angular momentum ($l \neq 0$) develops an MZM when Coulomb repulsion is high enough [35]. In this case, a magnetic field, RSOC, and even superconductivity are not needed either. Another interesting idea is to use profiled topological insulators [36], which do not require the RSOC or magnetic field.

A system similar to ours was considered in Ref. [37] numerically. Using DMRG, they showed that the mean-field approximation is not valid in a strong correlation regime ($U/t \leqslant 2$), and also MZMs can be produced in this regime. Analogous work in Ref. [38] showed that, due to strong correlation, the parameter space of a chemical potential magnetic field for the generation of the MZM increases. In fact, they even predicted that the MZM can be created only due to strong correlation—without a magnetic field. Our article differs from all the above works in the sense that we solve explicitly the corresponding Hamiltonian analytically using a su(2) coherent state representation of the Hubbard X^{pq} operators, and we show the presence of the MZM. In the same framework, we discuss the effect of RSOC on the system.

This article is structured as follows. In Sec. II we find the effective Hamiltonian for the physical system shown in Fig. 1. In Sec. III we derive the expression of the Hamiltonian when the spiral spin field is present in the wire. In Secs. IV and V
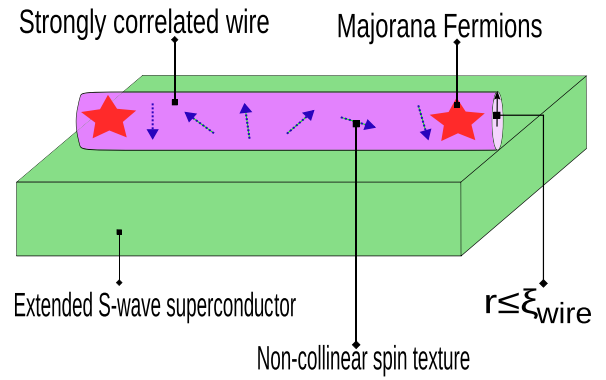
FIG. 1. A schematic of the system under consideration. A strongly correlated 1D nanowire is placed over a superconductor with an extended s-wave order parameter. Superconductivity is induced in the nanowire due to the proximity effect. The radius of the wire (r) is assumed to be smaller than the Cooper pair coherence length in the wire (ξ_{wire}): $r \lesssim \xi_{\text{wire}}$. The Majorana fermions appear at the end of the nanowire (stars) if a noncollinear spin texture is present in the wire.

we discuss the case when RSOC in the wire is both absent and present, respectively. In Sec. VI we calculate the thermodynamic free energy of the nanowire as a function of system parameters, and we discuss its consequences. In Sec. VII we propose experiments to observe the Majorana fermions and the schematics for device design. In Sec. VIII we summarize our results.

II. MODEL

The schematics of the system under consideration is shown in Fig. 1. Here, a strongly correlated 1D nanowire with RSOC is placed on a superconducting substrate. Due to the proximity of the wire to the superconductor, we assume tunneling of the Cooper pair into the wire (tunneling of a single electron is neglected due to the reasons discussed later). Under these assumptions, the total Hamiltonian of the wire will be

$$H = H_{1D} + H_\alpha + H_\Gamma,$$

where

$$H_{1D} = -t \sum_{i,\sigma} X_i^{\sigma 0} X_{i+1}^{0\sigma} + \text{H.c.} + \mu \sum_i X_i^{00},$$

$$H_\alpha = -\iota\alpha \sum_i X_i^{\sigma'0} X_{i+1}^{0\sigma} - X_i^{\sigma 0} X_{i+1}^{0\sigma'} + \text{H.c.},$$

$$H_\Gamma = \Gamma \sum_{i,\sigma} X_i^{\sigma 0} d_{i\sigma} + \text{H.c.} \tag{1}$$

Here, t is the electron hopping factor and μ is the chemical potential. σ is the electron spin, which can have only two quantum states $\uparrow$ and $\downarrow$. $X_i^{pq} = \langle p|q \rangle$ is the Hubbard operator, which represents the transition from the $|q\rangle$ state to the $|p\rangle$ state at the ith site. In the strong correlation regime, i.e., when Coulomb repulsion between electrons is infinitely large, only three states are allowed at each atomic site: $|\uparrow\rangle$, $|\downarrow\rangle$, or $|0\rangle$. For example, $X_i^{\uparrow 0}$ represent the transition from the empty state to the up-spin state at the ith site. In terms of usual electron

creation ($c_{i\sigma}^{\dagger}$), annihilation ($c_{i\sigma}$), and number ($n_{i\sigma} = c_{i\sigma}^{\dagger} c_{i\sigma}$) operators, the Hubbard operators are represented as

$$X_i^{0\sigma} = c_{i\sigma}(1 - n_{i\sigma'}), \quad X_i^{\sigma 0} = (1 - n_{i\sigma'})c_{i\sigma}^{\dagger},$$

$$X_i^{00} = X_i^{0\sigma} X_i^{\sigma 0} = c_{i\sigma}(1 - n_{i\sigma'})(1 - n_{i\sigma'})c_{i\sigma}^{\dagger}. \quad (2)$$

The above definition of Hubbard operators shows that the no double occupancy condition is satisfied. X_i^{00} gives the occupation number of the ith site. It should be remembered that the electron is created only if the ith site was empty initially. In the total Hamiltonian H, the H_{1D} part contains the kinetic energy and chemical potential of the wire.

H_α represents the RSOC in the wire. α is the Rashba parameter, which depends on the crystal electric field generated due to the breaking of the inversion symmetry [39]; quantitatively, $\alpha \sim 1$ eV [4]. H_Γ corresponds to the tunneling of electrons from the superconducting substrate to the wire with amplitude Γ. $d_{i\sigma}$ is the electron annihilation operator with spin σ at the ith site of the superconducting substrate. $X_i^{\sigma 0} d_{i\sigma}$ means the annihilation of the electron in the substrate and creation of the same in the wire. It is important to note that the Hubbard operators $X_i^{\sigma 0}$ transform themselves in the lowest (fundamental) representation of the SU(2) group [40], so that Eq. (1) represents a rotationally invariant interaction.

As the dimension and physical size of the wire are smaller than the substrate, it is natural to assume that the Fermi level of the superconductor greatly exceeds that of the wire, $k_F^{SC} \gg k_F^{wire}$. The large difference in Fermi levels allows the hybridization between them to be controlled mainly by the superconducting energy gap (Δ_{SC}) and Γ. For small Γ, i.e., for $\Gamma k_F^{SC} \ll \Delta_{SC}$, we can treat H_Γ perturbatively [3]. The first-order perturbation terms can be neglected, due to the suppression of the single-electron tunneling [41]. The second-order perturbation generates an effective Cooper pair hopping [42,43]. Due to the presence of strong correlation, one can discard the single-site spin-singlet s-wave pairing ($\Delta_{i,i}^{\uparrow\downarrow}$) contribution [44]. Therefore, on neighboring sites two types of spin pairing are possible: (i) spin-singlet extended s-wave pairing, and (ii) spin-triplet p-wave pairing. The corresponding second-order perturbed Hamiltonian is

$$\delta H_\Gamma \propto \sum_i \Delta_{i,i+1}^{\sigma\sigma'} \left(X_i^{\sigma 0} X_{i+1}^{\sigma'0} - X_i^{\sigma'0} X_{i+1}^{\sigma 0} \right)$$

$$+ \sum_i D_{i,i+1}^{\sigma\sigma'} \left(X_i^{\sigma 0} X_{i+1}^{\sigma'0} + X_i^{\sigma'0} X_{i+1}^{\sigma 0} \right)$$

$$+ \sum_{i,\sigma} D_{i,i+1}^{\sigma\sigma} X_i^{\sigma 0} X_{i+1}^{\sigma 0} + \text{H.c.} \quad (3)$$

Here, $D_{i,i+1}^{\sigma\sigma}$, $D_{i,i+1}^{\sigma\sigma'}$ are the p-wave order parameters, and $\Delta_{i,i+1}^{\sigma\sigma'}$ is the extended s-wave order parameter. In the low-energy limit we can approximate the order parameters through ground-state expectation values:

$$D_{i,i+1}^{\sigma\sigma} = \langle d_{i,\sigma} d_{i+1,\sigma} \rangle,$$

$$D_{i,i+1}^{\sigma\sigma'} = \langle d_{i,\sigma} d_{i+1,\sigma'} + d_{i,\sigma'} d_{i+1,\sigma} \rangle,$$

$$\Delta_{i,i+1}^{\sigma\sigma'} = \langle d_{i,\sigma} d_{i+1,\sigma'} - d_{i,\sigma'} d_{i+1,\sigma} \rangle. \quad (4)$$

In Eq. (4) the spin-triplet p-wave order parameters are symmetric in spin ($D_{i,i+1}^{\sigma\sigma'} = D_{i,i+1}^{\sigma'\sigma}$), but antisymmetric in

space ($D_{i,i+1}^{\sigma\sigma'} = -D_{i+1,i}^{\sigma\sigma'}$). On the other hand, the extended s-wave order parameters are antisymmetric in spin ($\Delta_{i,i+1}^{\sigma\sigma'} = -\Delta_{i,i+1}^{\sigma'\sigma}$), but symmetric in space ($\Delta_{i,i+1}^{\sigma\sigma'} = \Delta_{i+1,i}^{\sigma\sigma'}$). Usually p-wave pairing in superconductors is quite rare and unstable. On the other hand, the extended s-wave pairing is predicted in high T_c iron-based superconductors [32,45]. Hence, from now on we assume that the substrate develops only extended s-wave pairing. Considering the above discussion, we can approximate

$$\delta H_\Gamma = \Delta \sum_i X_i^{\sigma 0} X_{i+1}^{\sigma'0} - X_i^{\sigma'0} X_{i+1}^{\sigma 0} + \text{H.c.} \quad (5)$$

Here Δ is the induced superconducting gap in the wire. Its value can be estimated through $\Delta \approx \Gamma^2 / k_F^{SC} \Delta_{SC}$. We have assumed a spatially independent order parameter $\Delta_{i,i+1}^{\sigma\sigma'} \equiv \Delta_{SC}$. Combining Eqs. (1) and (5), we write the effective Hamiltonian of the wire:

$$H_{\text{eff}} = -t \sum_{i,\sigma} X_i^{\sigma 0} X_{i+1}^{0\sigma} - \iota\alpha \sum_i X_i^{\sigma'0} X_{i+1}^{0\sigma} - X_i^{\sigma 0} X_{i+1}^{0\sigma'}$$

$$+ \Delta \sum_i X_i^{\sigma 0} X_{i+1}^{\sigma'0} - X_i^{\sigma'0} X_{i+1}^{\sigma 0} + \text{H.c.} + \mu \sum_i X_i^{00}. \quad (6)$$

To solve the Hamiltonian, Eq. (6), the su(2|1) path integral representation of the partition function will be used. This is possible due to the existence of an injective mapping between Hubbard operators $X^{\sigma\sigma'}$ and their su(2|1) coherent-state symbols [29,46,47] (also known as Berezin symbols [48]):

$$X^{\sigma\sigma'}(z, \xi) \equiv \langle z, \xi | X^{\sigma\sigma'} | z, \xi \rangle. \quad (7)$$

Here z and ξ are the complex even and odd Grassmann parameters, respectively. The state $|z, \xi\rangle$ is defined as

$$|z, \xi\rangle \equiv (1 + \bar{z}z + \bar{\xi}\xi)^{-1/2} \exp(z X^{\downarrow\uparrow} + \xi X^{0\uparrow})|\uparrow\rangle$$

$$= (1 + \bar{z}z + \bar{\xi}\xi)^{-1/2}(|\uparrow\rangle + z|\downarrow\rangle + \xi|0\rangle). \quad (8)$$

The above representation was found by acting with the lowering superspin operators $X^{\downarrow 0}$ and $X^{\downarrow\uparrow}$ on the highest weight state $|\uparrow\rangle$. For a complete exposition on this subject, please see Refs. [46,49]. Physically, z represents the spinful bosonic fields, and ξ represents the spinless charged fermionic fields [49,50]. In this new representation, and using the change of variables,

$$\xi \rightarrow \frac{\xi}{\sqrt{1 + |z|^2}}, \quad z \rightarrow z,$$

the effective Hamiltonian Eq. (6) will be

$$H_{\text{eff}}(z, \xi) = -t \sum_i \xi_i \bar{\xi}_{i+1} a_{i,i+1} + \iota\alpha \sum_i \xi_i \bar{\xi}_{i+1} \alpha_{i,i+1}^*$$

$$- \Delta \sum_i \xi_i \xi_{i+1} \Delta_{i,i+1}^* + \text{H.c.} + \mu \sum_i \bar{\xi}_i \xi_i, \quad (9)$$

where

$$a_{i,i+1} \equiv \frac{1 + \bar{z}_i z_{i+1}}{\sqrt{(1 + |z_i|^2)(1 + |z_{i+1}|^2)}}, \tag{10a}$$

$$\alpha_{i,i+1}^* \equiv \left[\frac{z_i - \bar{z}_{i+1}}{\sqrt{(1 + |z_i|^2)(1 + |z_{i+1}|^2)}} \right]^*, \tag{10b}$$

$$\Delta_{i,i+1}^* \equiv \left[\frac{z_i - z_{i+1}}{\sqrt{(1 + |z_i|^2)(1 + |z_{i+1}|^2)}} \right]^*. \tag{10c}$$

In the second quantization language, ξ_i ($\bar{\xi}_i$) creates (annihilates) a spinless fermion at the ith site. Similarly, z_i ($\bar{z}_i$) creates (annihilates) a spinful boson at the ith site. In Eq. (9) the ξ and z degrees of freedom emerge as low-energy degrees of freedom.

One can absorb the electron hopping and RSOC terms in Eq. (9) into a single effective term. In this case, the Hamiltonian, Eq. (9), transforms to

$$H_{\mathrm{eff}}(z, \xi) = - \sum_i \bar{\xi}_i \xi_{i+1} (t\, a_{i,i+1}^* + \iota \alpha\, \alpha_{i,i+1})$$
$$- \Delta \sum_i \bar{\xi}_i \bar{\xi}_{i+1} \Delta_{i,i+1}^* + \mathrm{H.c.} + \mu \sum_i \bar{\xi}_i \xi_i. \tag{11}$$

In effect, electron hopping acquires a phase that is a complex function of the spin field. One can define the modified hopping as

$$\tilde{t}_i = \sqrt{(t\, a_{i,i+1}^*)^2 + (\alpha\, \alpha_{i,i+1})^2} \, \exp\left[\iota \arctan\left(\frac{\alpha\, \alpha_{i,i+1}}{t\, a_{i,i+1}^*} \right) \right]. \tag{12}$$

III. HAMILTONIAN FOR SPIRAL SPIN FIELDS

While treating the real systems, it is instructive physically to treat the dynamic spin fields $z_i(t)$ in terms of the spin covariant symbols [46]:

$$S_i^+ = \frac{z_i}{1 + |z_i|^2}, \quad S_i^- = \frac{\bar{z}_i}{1 + |z_i|^2}, \quad S_i^z = \frac{1}{2}\left(\frac{1 - |z_i|^2}{1 + |z_i|^2} \right). \tag{13}$$

The corresponding expressions for $S_i^x = S_i^+ + S_i^-$ and $S_i^y = -\iota(S_i^x - S_i^y)$ can be easily found. In strongly correlated electronic systems, the dynamics of the effective spin field is much slower than that of the fermionic fields [51]. Because of this, we can apply the mean-field approximation to the spin system (from the point of view of the fermions). In other words, the picture where spinless fermions travel in the static background of the spin field is fully applicable. One of the main differences between our approach and the previous works related to the 1D topological superconductors [9,13,18,52] is that we first derive our effective Hamiltonian taking full account of the strong correlation effects, and only then do we apply the mean-field approximation. Contrary to previous works, the mean-field approximation is applied to the Hamiltonian right from the beginning. In fact, using density matrix renormalization group it was explicitly shown that

the usual mean field model fails when strong correlation is present [37].

We consider a spin field of the form

$$\vec{S}_i = \left(S_i^x, S_i^y, S_i^z \right) = \frac{1}{2}(\cos\theta_i, \sin\theta_i, 0). \tag{14}$$

Physically it represents the rotating spin vector on the xy plane; the z component of the spin is zero. θ_i is the angle on the xy plane. It is related to the spatial coordinate through the relation $\theta_i = \vec{q} \cdot \vec{r}_i$, where $\vec{q}$ is the spin wave vector and $\vec{r}_i$ is the position vector. Substituting Eq. (14) in Eq. (13) it is easy to see that $z_i = e^{\iota\theta_i}$. Further, using this z_i in Eqs. (10a), (10b), and (10c), one will find

$$a_{i,i+1}^* = e^{-\iota(\theta_{i+1} - \theta_i)/2} \quad \cos\frac{(\theta_{i+1} - \theta_i)}{2},$$
$$\alpha_{i,i+1} = \iota e^{-\iota(\theta_{i+1} - \theta_i)/2} \quad \sin\frac{(\theta_{i+1} + \theta_i)}{2},$$
$$\Delta_{i,i+1} = -\iota e^{\iota(\theta_{i+1} - \theta_i)/2} \quad \sin\frac{(\theta_{i+1} - \theta_i)}{2} \, e^{\iota\theta_i}. \tag{15}$$

Substituting Eq. (15) in Eq. (11), and soon after that making the gauge transformations $\xi_i \to \xi_i e^{\iota(\theta_i/2 - \pi/4)}$, the effective Hamiltonian can be written as

$$H_{\mathrm{eff}} = -t \sum_i \bar{\xi}_i \xi_{i+1} \cos\frac{(\theta_{i+1} - \theta_i)}{2}$$
$$+ \alpha \sum_i \bar{\xi}_i \xi_{i+1} \sin\frac{(\theta_{i+1} + \theta_i)}{2}$$
$$- \Delta \sum_i \bar{\xi}_i \bar{\xi}_{i+1} \sin\frac{(\theta_{i+1} - \theta_i)}{2} + \mathrm{H.c.} + \mu \sum_i \bar{\xi}_i \xi_i. \tag{16}$$

In a limiting case, one can assume that the rotation of the spin through neighboring sites $\theta_{i+1} - \theta_i \equiv \theta$ is constant. This spin structure is known as the spiral spin structure. A schematic of it is shown in Fig. 2. The Hamiltonian for the spiral spin structure then becomes

$$H_{\mathrm{eff}} = -t \sum_i \bar{\xi}_i \xi_{i+1} \cos\frac{\theta}{2} + \alpha \sum_i \bar{\xi}_i \xi_{i+1} \sin\left(\theta_i + \frac{\theta}{2}\right)$$
$$- \Delta \sum_i \bar{\xi}_i \bar{\xi}_{i+1} \sin\frac{\theta}{2} + \mathrm{H.c.} + \mu \sum_i \bar{\xi}_i \xi_i. \tag{17}$$

The Rashba term is now real and oscillating.

Before further discussion, an explanation of why we considered the spiral spin texture is necessary. The spiral spin texture is not new and it has been observed in other systems, especially in heterostructures where magnetic adatoms are placed over superconducting substrates [9,10]. In these systems, strong RSOC [53], together with the RKKY interaction [54], are responsible for generating spiral spin texture. In fact, it can be shown that the tight-binding Hamiltonian of a 1D wire with spin-orbit coupling is equivalent to the tight-binding Hamiltonian with a rotating magnetic field [55]. This result is valid only when the e-e interaction is small ($U \ll t$). When the e-e interaction is strong, the Hamiltonian cannot be transformed in this way. This is due to the fractionalization of the electronic degrees of freedoms into a separate
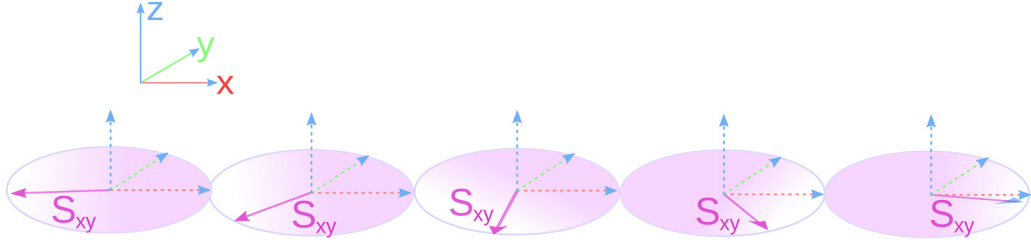
FIG. 2. Spiral spin structure found from Eq. (14) by taking $\theta_{i+1} - \theta_i = \theta$ as constant.

spinless fermionic field (charge) and a spinful bosonic field (spin).

The mechanisms for emergence of the spiral spin texture in the case of weak interactions are not applicable to the case of strong correlations. Therefore, we suggest the following mechanisms and approximations for the emergence of the spiral spin texture. For the strong e-e interaction, nearly localized effective spins emerge at individual sites. The effective spinful bosonic field is generated by Hubbard operators. A crucial observation is that the operators $X^{\sigma 0}$ transform in the spinor (fundamental) representation of the SU(2) group [40]. Because of this, the local spin operators that describe the effective spin degrees of freedom of strongly correlated electrons can be written as

$$\vec{Q}_i := X_i^{\dagger} \vec{\sigma} X_i, \tag{18}$$

where $X_i := (X_i^{0\uparrow}, X_i^{0\downarrow})^T$. It can be checked that a set of spin operators $\vec{Q}$ spans the su(2) algebra. The explicit coherent-state symbols of those operators can be found in Ref. [49]. Physically we have the effective system where at each lattice site sits a classical spin with $S = 1/2$, and in this spin background itinerant spinless fermions travel through the lattice. The nearly localized spins create a dynamical spin field for which the internal energy of the system is lowest.

Since the background spin field is generated dynamically, it is natural to assume that the system chooses the spin configuration for which the internal energy is lowest. Keeping this in mind, for analysis of the properties of the Hamiltonian, one can start with any noncollinear spin structure, however for general complex spin textures—e.g., for skyrmions, hopfions, etc,—the resulting Hamiltonian, Eq. (11), becomes too complex to be solved analytically. Hence, some assumptions are in order. First, we assume that the z component of the spin is zero; physically, this means that the spin rotates only on the xy plane. This was motivated by the fact that the spin projection along the z-axis does not play any role in determining the topological properties of the system for not too large spins S [56]; this means that only the spin rotations on the xy plane are important. Secondly, we assume that the rotation of the spin projection on the xy plane between two neighboring sites is constant. It is motivated by two facts: (i) a constant rotation angle—which corresponds to the spiral spin texture—has been observed in numerous experiments [8–10], and (ii) in this case the Hamiltonian takes a very simple form, which turns out to be solvable analytically.

IV. ABSENCE OF RSOC ($\alpha = 0$)

First we analyze Eq. (17) when the RSOC is absent, i.e., we take $\alpha = 0$. The effective Hamiltonian in this case becomes

$$H_{\text{eff}}^{\text{Kitaev}} = -t \sum_i \bar{\xi}_i \xi_{i+1} \cos\frac{\theta}{2} - \Delta \sum_i \bar{\xi}_i \bar{\xi}_{i+1} \sin\frac{\theta}{2}$$
$$+ \text{H.c.} + \mu \sum_i \bar{\xi}_i \xi_i. \tag{19}$$

This Hamiltonian does not break time-reversal symmetry, as $H_{\text{eff}}^{\text{K}} = (H_{\text{eff}}^{\text{K}})^*$. In this sense, it is analogous to Kitaev's toy model of topological superconductivity [2,57]. In fact, analogous to Kitaev's toy model, we also find that both the trivial and the topological phases depend on the specific values of t, Δ, μ, and θ. When there is no superconductivity, the system is gapped for $|\mu| > 2t \cos(\theta/2)$, but it is gapless when $|\mu| < 2t \cos(\theta/2)$. However, when superconductivity is itself present, due to the particle hole symmetry, a topological phase appears for $|\mu| < 2t \cos(\theta/2)$. The phase diagram of $H_{\text{eff}}^{\text{Kitaev}}$, and its dependence on θ—physically, θ represents the rotation of the spin projection through neighboring sites— is shown in Fig. 3. The main difference between the phase diagrams shown in Fig. 3, and the original phase diagram of the Kitaev chain [2], is the emergence of the new parameter θ in the effective Hamiltonian. It can be observed that with the increase in θ the area of the topological phase in the μ-t phase plane decreases. This is due to the decrease in the electron hopping parameter $t \cos(\theta/2)$. The boundary between the topological and the trivial phase in the $|\mu|/t$-θ phase space is given by the condition $|\mu|/t < 2 \cos(\theta/2)$. The corresponding phase diagram is shown in Fig. 3(d). In this figure we observe that, when $\theta = 0$, i.e., for the ferromagnetic state, the system behaves either as a simple metal or as an insulator depending on the relative value of μ [58]. The system loses its topological property at $\theta = 0$ due to the disappearance of the superconducting gap. In effect, the system loses the particle-hole symmetry, which in the first place gives rise to the topological phase. This is expected physically since the underlying extended s-wave superconducting state should not survive in a ferromagnetic background. On the other end, when $\theta = \pi$, i.e., for an antiferromagnetic state, the system behaves as an usual Mott insulator. The hopping of the electrons becomes identically zero, and this represents a state in which the fermionic particles are frozen in their lattice sites. From the band theory point of view, the superconducting gap never closes even if μ is modified, when $\theta = \pi$. This means that the MZM cannot be created, since in such a state
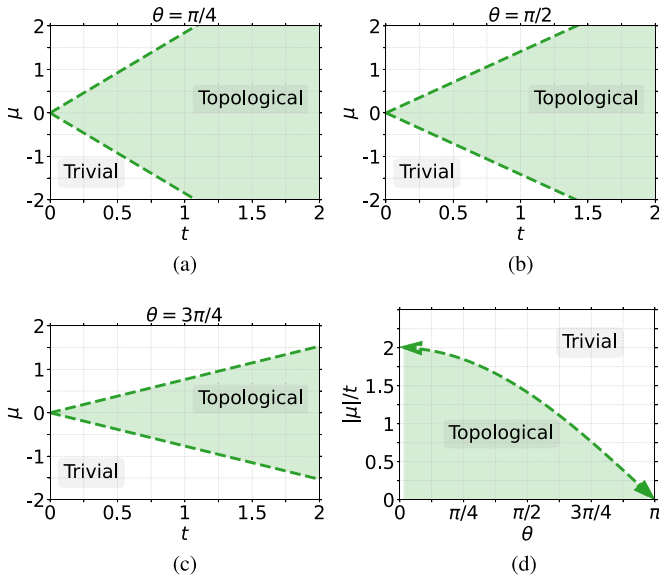
FIG. 3. (a), (b), (c) Dependence of trivial and topological phase on the angle of the rotation of the spin through neighboring sites (θ). The topological phase appears when $|\mu| < 2t \cos(\theta/2)$ is satisfied. The range of parameters μ and t, for which topological phase occurs, decreases with increase in θ. (d) The condition $|\mu/t| < 2\cos(\theta/2)$ determining the topological phase is plotted. The area for the topological phase in parameter space is largest when spins on neighboring atoms are almost aligned along the same direction ($\theta > 0$). For ferromagnetic ordering ($\theta = 0$) the topological phase vanishes as the superconducting gap [$\Delta \sin(\theta/2)$] also vanishes. For anti-ferromagnetic ordering ($\theta = \pi$) the topological phase vanishes, because electron hopping becomes zero [$t \cos(\theta/2)$]. The arrow marks on the boundary of the topological and trivial phase near $\theta = 0, \pi$ represent the fact that the topological phase survives as $\theta \to 0$ and $\theta \to \pi$, however at $\theta = 0, \pi$ the topological phase is absent.

Majorana fermions only emerge during the closing and the reopening of the band gap.

To support the previous results, we numerically diagonalize the real-space Hamiltonian Eq. (19) for a chain of 35 atoms. First the energy modes are calculated for different μ keeping $\theta = \pi/4$ [Fig. 4(a)] and $\theta = 3\pi/4$ [Fig. 4(b)] constant. One can clearly see the zero-mode energy and their splitting as μ increases. In Figs. 4(c) and 4(d) we analyze the dependence of the energy modes on θ while the chemical potential μ is kept constant. In these figures, one can see that when $\theta \to 0$ and $\theta = \pi$, zero mode energy is absent as was predicted in Fig. 3(d). If we compare Figs. 4(c) and 4(d) with Fig. 2(a) of Ref. [9], then we find an analogous dependence on the magnetic field; in our case, θ plays the same role as the magnetic field in Ref. [9]. Next, we discuss the effect of θ on the energy spectrum. Using Nambu spinors in momentum space, the Hamiltonian Eq. (19) can be written in the usual Bogoliubov–de Gennes form

$$H_{\text{eff}}^{\text{Kitaev}}(k) = \frac{1}{2} \sum_{k \in \text{BZ}} \Psi_k^\dagger \, \mathcal{H}_k \, \Psi_k,$$
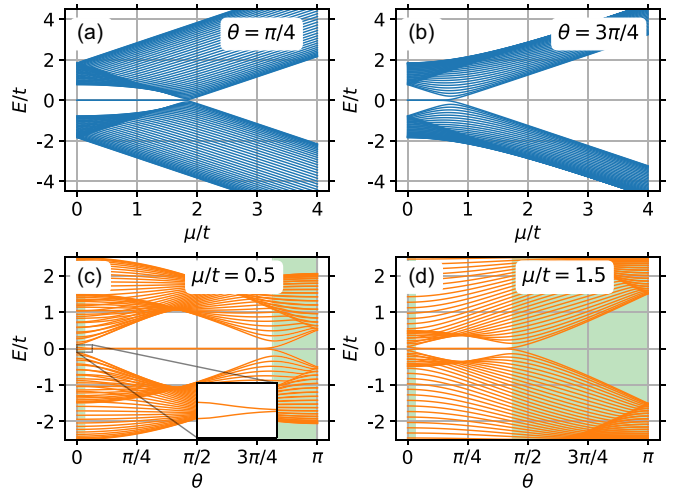
FIG. 4. Dependence of real-space energy modes on μ and θ for a chain of 35 atoms. (a), (b) Energy modes are calculated by numerically diagonalizing the Hamiltonian Eq. (19) for $\theta = \pi/4$ and $3\pi/4$. We fixed the superconducting gap $\Delta = 0.5t$. The zero-mode energy is present up to values of $\mu/t = 2 \cos(\theta/2)$. (c), (d) Dependence of energy modes on θ for $\mu = 0.5t$ and $1.5t$. The inset in (c) shows the absence of zero-mode energy at $\theta \to 0$.

where

$$\Psi_k^\dagger \equiv [\xi_k, \bar{\xi}_{-k}],$$

$$\mathcal{H}_k \equiv \begin{bmatrix} 2t \cos \frac{\theta}{2} \cos ka - \mu & 2\Delta \sin \frac{\theta}{2} \sin ka \\ 2\Delta \sin \frac{\theta}{2} \sin ka & 2t \cos \frac{\theta}{2} \cos ka - \mu \end{bmatrix}. \tag{20}$$

Here, k is the crystal momentum, and a is the distance between two near-neighbor lattice sites. The single-mode energy dispersion can now be easily calculated:

$$E(k) = \pm \sqrt{\left(2t \cos \frac{\theta}{2} \cos ka - \mu \right)^2 + \left(2\Delta \sin \frac{\theta}{2} \sin ka \right)^2}. \tag{21}$$

If one compares the energy dispersion of Eq. (21) with the energy dispersion of Kitaev's toy model [see Eq. (13) of Ref. [2] again], there is only a single difference: in Eq. (21) the extra parameter θ appears explicitly in our energy dispersion. The dependence of energy dispersion for different combinations of Δ, μ, and θ is shown in Figs. 5 and 6.

In Figs. 5(a), 5(b) and 5(c) the evolution of the energy dispersion is shown for $\theta = \pi/4$, $\pi/2$, and $3\pi/4$, while the superconducting gap is kept constant ($\Delta = 0.7t$), and the chemical potential is varied as a function of t ($\mu = 2t, 1.5t, 0.7t, 0$). As is well known, one of the properties of the topological superconductors is its sensitivity to the closing and to the reopening of the energy gap at $k = 0, \pm\pi$ when we tune μ. In Kitaev's toy model this takes place precisely at $\mu = \pm 2t$. However, in our case the gap closes for $\mu = \pm 2t \cos(\theta/2)$—it evolves with θ. The values of μ/t where the gap closes for a given θ are plotted in Fig. 5(d). Similarly, in Figs. 6(a), 6(b) and 6(c) the energy dispersion is shown for $\theta = \pi/4$, $\pi/2$, and $3\pi/4$, while the chemical potential is kept constant
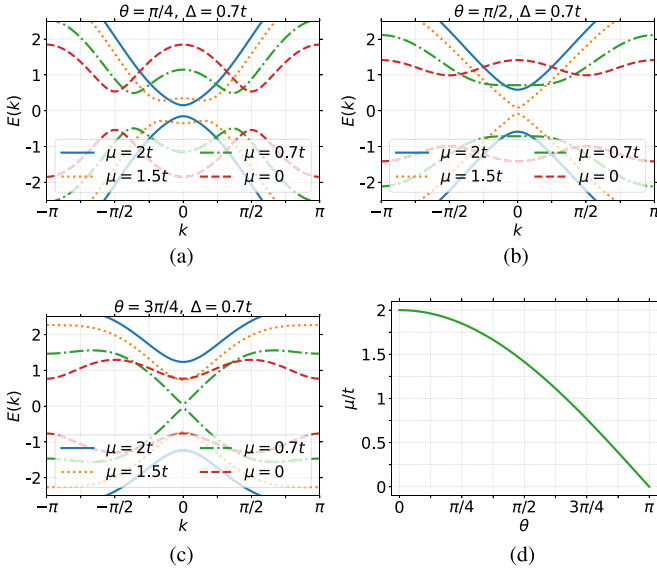
FIG. 5. (a), (b), (c) Evolution of the energy dispersion, Eq. (21), as the superconducting gap is kept constant ($\Delta = 0.7t$), and chemical potential is decreased (μ changes from $2t$ to 0) for $\theta = \pi/4$, $\theta = \pi/2$, and $\theta = 3\pi/4$. (d) The values of $|\mu|/t$ at which the bulk gap closes at $k = 0$ for a given value of θ. The values are found by using the condition $\theta = 2 \arccos(|\mu|/2t)$.

($\mu = 1t$), and the superconducting gap is varied ($\Delta = 0.1t$, $0.3t$, $0.5t$, $0.6t$). As is expected for $\theta = \pi/4$, the spectrum is defined by the electron hopping term $[2t \cos(\theta/2) \cos k]$; the superconducting term has little effect as $[2t \sin(\theta/2) \sin k]$ is very small. However, for $\theta = 3\pi/4$ the spectrum is defined by the superconducting term. As the dispersion is a function
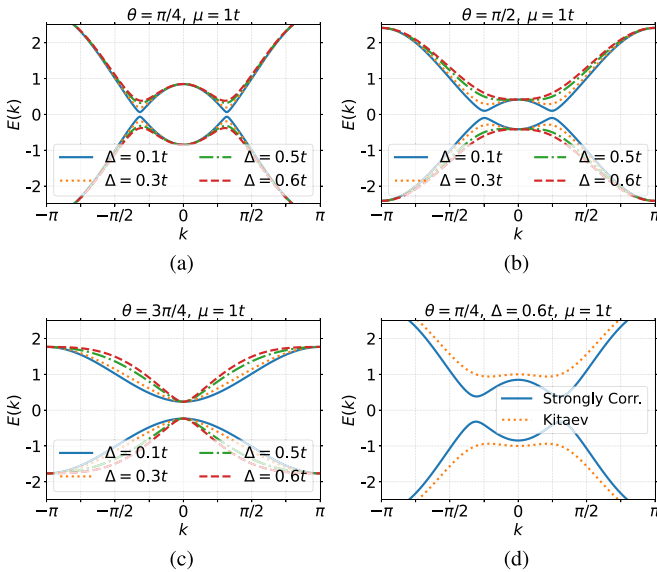
FIG. 6. (a), (b), (c) Evolution of the energy dispersion, Eq. (21), as the chemical potential is kept constant ($\mu = 1t$), and the superconducting gap is increased ($\Delta = 0.1t$, $0.3t$, $0.5t$, $0.6t$) for $\theta = \pi/4$, $\theta = \pi/2$, and $\theta = 3\pi/4$. (d) Comparison of the energy dispersion for the strongly correlated Hamiltonian, Eq. (19), and the Kitaev's toy model [2] at $\mu = 1t$, $\Delta = 0.6t$, and $\theta = \pi/4$.
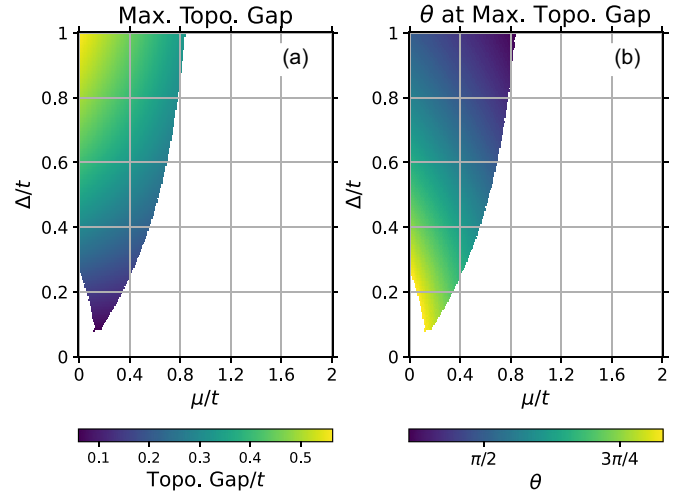
FIG. 7. Dependence of the topological gap on θ, μ, Δ calculated numerically using dispersion Eq. (21). (a) Values of the maximum topological gap energy for different μ and Δ. (b) Corresponding values of θ for which the maximum topological gap occurs. The lines show the contour line of equal values of the topological gap (a) and θ (b). In this figure we have not shown the values of $0 < \theta < \pi/6$ or $\pi - \pi/6 < \theta < \pi$ and corresponding topological gaps.

of θ, μ, and Δ, the topological gap will also depend on these parameters. In Fig. 7 we showed the highest topological gap and corresponding θ for a given value of μ and Δ. In Fig. 7(b) we show the value of θ for which the maximum topological gap results; the corresponding topological gap energy is shown in Fig. 7(a). In both these figures we did not show the value of μ and Δ for which θ in the vicinity of 0 and π—i.e., where $0 < \theta < \pi$ or $\pi - \pi/6 < \theta < \pi$—as at these values of θ either the highest topological gap is almost negligible or the system is an insulator. Both of these cases are of no interest to us. However, it should be kept in mind that the values of μ and Δ for which the topological gap is not shown in Fig. 7 does not mean the topological phase is always absent there, it just means that the highest topological phase appears in the aforementioned limits of θ.

The angle $\theta = \vec{q} \cdot (\vec{r}_i - \vec{r}_{i+1}) = \vec{q} \cdot \vec{a}$, where $\vec{a}$ is a lattice spacing and $\vec{q}$ is a spin spiral modulation vector, appears as a control parameter. It can in principle be tuned by changing a. However, such a change affects the other parameters in the Hamiltonian as well. One could alternatively try to change the modulation vector $\vec{q}$ by applying an external modulated field as discussed in Sec. VII. It is still not quite clear, however, how the tunability of θ could be realized in an efficient way.

A comment is in order regarding the related work of Ref. [59]. If one compares our Hamiltonian, Eq. (20), with Eq. (20) of Ref. [59], they are identical. However, there are a few fundamental differences in what the two models truly represent. In Ref. [59] the heterostructures are produced by the magnetic adatoms on a superconductor, while in our work we consider a strongly correlated 1D nanowire on the superconductor. In the magnetic adatom superconductor heterostructures the whole physics is directly related to the YSR states, while in our system the physics depends on the proximity effect induced by the superconductivity and by the

chemical potential of the nanowires. In this sense they are completely different systems. A priori it is not obvious they can be represented by one and the same low-energy theory. This only happens in the limit where on-site Coulomb repulsion is infinite. If one goes away from that limit, the relevant theories differ from each other accordingly. In our work, we have also considered the effect of the RSOC, which was not taken into account in Ref. [59].

V. PRESENCE OF RSOC ($\alpha \neq 0$)

When the RSOC is present, i.e., when ($\alpha \neq 0$), we can observe in the $|\mu|/t$-θ phase plane the region in which the topological phase manifest is contracted with the increase in the value of α. To show this more explicitly, we rewrite the effective Hamiltonian, Eq. (16), as

$$H_{\text{eff}}(z, \xi) = - \sum_i \tilde{t}_i \, \bar{\xi}_i \xi_{i+1} - \Delta \sum_i \bar{\xi}_i \bar{\xi}_{i+1} \sin \frac{\theta}{2}$$
$$+ \text{H.c.} + \mu \sum_i \bar{\xi}_i \xi_i,$$

where

$$\tilde{t}_i \equiv \left[t \cos \left(\frac{\theta}{2} \right) - \alpha \sin \left(\theta_i + \frac{\theta}{2} \right) \right] \qquad (22)$$

is the modified hopping term. Interestingly, it is spatially oscillating through $\sim \alpha \sin \theta_i$. Equations (22) and (19) are analogous to each other, apart from the modified hopping parameter. Therefore, the boundary of the topological phase can be established by the same process—one can canonically represent the fermionic ξ_i operators in terms of the Majorana fermions, and apply the limiting conditions to find the associated topological phase boundary (see Ref. [2]). The resulting condition for the topological phase is then $|\mu| < \text{Min}(2\tilde{t}_i)$. Explicitly, we can write

$$|\mu| < 2 \left(t \cos \frac{\theta}{2} - |\alpha| \right). \qquad (23)$$

The corresponding values for μ, t, and θ which determine both the topological and trivial phases for different values of α are displayed in Fig. 8. We note that the parameter range for the topological phase decreases gradually as we increase the magnitude of α. When $\alpha \geqslant t \cos(\theta/2)$ the topological phase is completely absent. Therefore, the RSOC and nonalignment of the spin vectors negatively affect the topological phase in a strongly correlated regime. We can conclude that for strongly correlated wire the RSOC does not add new physics to the problem.

VI. SUPERCONDUCTING CONDENSATION ENERGY

The results found in the previous sections were applicable when the spiral spin texture is present in the system. In Eq. (21) it was explicitly shown that the single-mode energy depends also on the spin rotation angle θ. However, as mentioned before, the background spin field is dynamic in nature. This means that θ changes as we change the global system parameters μ and Δ. These two parameters are essential for the determination of the lowest internal energy (U_{Internal}). The
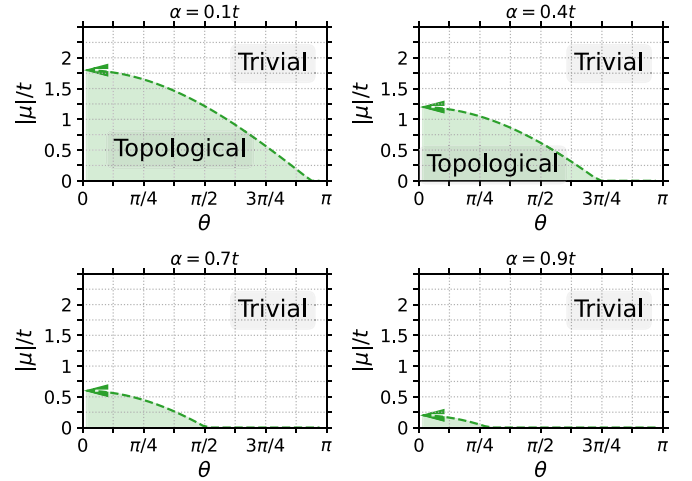
FIG. 8. Dependence of trivial and topological phase on θ for different Rashba interaction $\alpha = 0.1t$, $0.2t$, $0.7t$, and $0.9t$. The plotted condition for topological phase is found from Eq. (23): $|\mu|/t = 2 \cos(\theta/2) - |\alpha|/t$.

internal energy is found by summing over the energies of all the occupied states:

$$U_{\text{Internal}} = \sum_{k \in \text{BZ}} E(k) f[E(k), \mu],$$

where

$$f[E(k), \mu] \equiv \frac{1}{e^{[E(k) - \mu]/k_B T} + 1}. \qquad (24)$$

$f[E(k), \mu]$ is the Fermi-Dirac distribution, $k_B = 8.6 \times 10^{-5} \, \text{eV} \, \text{K}^{-1}$ is the Boltzmann constant, and T is the temperature. In our calculation, we take $T \approx 0 \, \text{K}$. The summation in Eq. (24) is taken over the whole Brillouin zone $k \in [-\pi, \pi]$. Although U_{Internal} is an important characteristic of the system, for superconducting systems the condensation energy $E_{\text{Cond.}}$ is of importance. Physically it represents the decrease in internal energy in the superconducting states $U_{\text{Internal}}(\Delta \neq 0)$ compared to the normal state $U_{\text{Internal}}(\Delta = 0)$. It is defined as [see Sec. 3.4.2 of Ref. [60]]

$$E_{\text{Cond.}} = U_{\text{Internal}}(\Delta = 0) - U_{\text{Internal}}(\Delta \neq 0). \qquad (25)$$

Positive $E_{\text{Cond.}}$ means decreases in internal energy in superconducting states compared to nonsuperconducting states, and *vice versa*. As it is always preferable that the ground state of the system has the lowest possible energy, the system always tries to be in that state where the $E_{\text{Cond.}}$ is highest.

In Fig. 9 we show the dependence of the condensation energy on θ for constant $\Delta = 0.5t$, and for different μ values. The energies are normalized in these figures. As positive $E_{\text{Cond.}}$ is preferable, we search for local maxima in these plots. It should be remembered that the system has topological properties only when $\theta \neq 0, \pi$; this is a necessary but not sufficient condition. The second condition is

$$\theta < \theta_{\text{Topo}} \equiv 2 \, \arccos \left| \frac{\mu}{2t} \right|. \qquad (26)$$

This gives the upper boundary θ_{Topo} for a topological phase; θ_{Topo} is a function of μ. In Fig. 9 the values of θ_{Topo} obtained
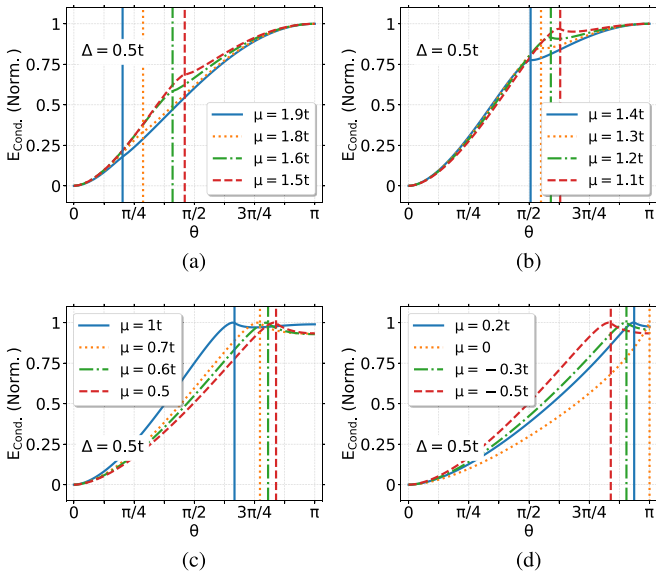
FIG. 9. (a), (b), (c), (d) Dependence of the condensation energy ($E_{\text{Cond.}}$) on θ for constant superconducting gap ($\Delta = 0.5t$) as the chemical potential ($2t > \mu > 0$) decreases. The $E_{\text{Cond.}}$ is found by numerically integrating Eq. (24) over Brillouin zone $k \in [-\pi, \pi]$ and later applying Eq. (25). The $E_{\text{Cond.}}$ for different μ, Δ are normalized. The θ_{Topo} found from Eq. (26) is plotted as the vertical bar. Values of θ on the left of this bar where maxima occur have topological phase. Hence, if the energy maxima lie on the left of this vertical bar (but $\theta \neq \pi$), then the system thermodynamically resides in the topological phase.

from Eq. (26) are displayed as vertical lines. Therefore, if a global or local maximum lies on the left of the vertical bar and does not occur at $\theta = 0$, then the system will thermodynamically acquire a topological phase. In Fig. 10 we show the condensation energy dependence on θ for several values of μ and Δ. The values of θ found from Eq. (26) are shown as the vertical line. As was mentioned before, the following two conditions are sufficient and necessary for the emergence of the topological phase thermodynamically: (i) $\theta \in 0, \pi$, (ii) $\theta < \theta_{\text{Topo}}$; θ being the angle where the maxima of $E_{\text{Cond.}}$ occurs. In Fig. 11 we plot the values of μ and Δ which satisfy the aforementioned conditions thermodynamically. The shaded regions represent the topological phase, while the unshaded regions represent the trivial no topological phase. The color coding in the figure represents the value of θ where maximum energy occurs thermodynamically.

In addition to Fig. 11, in Fig. 12 we also show the first-order differentiation of the condensation energy $dE_{\text{Cond.}}/d\theta$ for constant $\mu = 1.5t$ and different $0.1 \leqslant \Delta \leqslant 0.9$. We observe that, as was expected from Fig. 10(a), with an increase in Δ the energy maximum ($dE_{\text{Cond.}}/d\theta = 0$) shifts toward the right. This signals a transition to the nontopological phase.

While comparing Fig. 10(a) with Fig. 7 one might think they contradict each other. However, it should be remembered that in Fig. 7 we showed the values of μ and Δ for which the highest energy gap occurs away from $\theta \approx 0, \pi$; if the highest energy occurs in the vicinity of $\theta \approx 0, \pi$ we did not show them. For example, the missing values of $\mu = 1.5t$ in Fig. 7 do not mean that the topological gap is absent there; it just
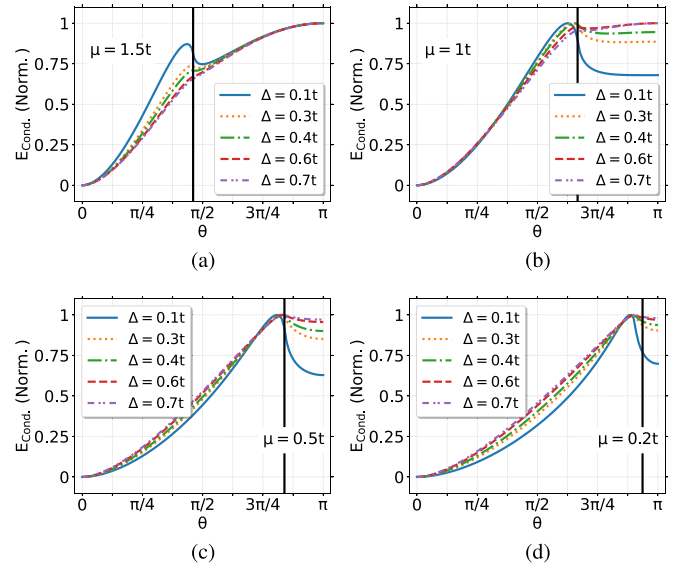
FIG. 10. (a), (b), (c), (d) Dependence of the condensation energy ($E_{\text{Cond.}}$) on θ for constant chemical potential (μ) as the superconducting gap (Δ) increases. The $E_{\text{Cond.}}$ is found by numerically integrating Eq. (24) over Brillouin zone $k \in [-\pi, \pi]$ and later applying Eq. (25). The $E_{\text{Cond.}}$ for different μ, Δ are normalized. The θ_{Topo} found from Eq. (26) is plotted as vertical bar. Values of θ on the left of this bar at which the maxima occur have topological phase. Hence, if the energy maxima lie on the left of this vertical bar (but $\theta \neq \pi$) then the system thermodynamically resides in the topological phase.

means that for $\mu = 1.5t$ the "*highest*" topological gap appears in the vicinity of $\theta \approx 0, \pi$. However, at other θ, although the topological gap might not be the highest, the topological phase is present. This is exactly the case in Fig. 10(a). Besides, one should keep in mind that in Fig. 10 we have shown the normalized values of the internal energy.

The main physical conclusion from this section is that by modifying the chemical potential, we can drive the system
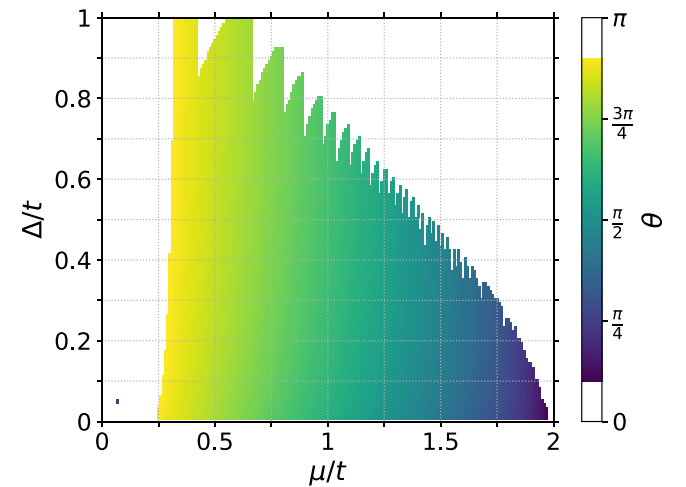
FIG. 11. Phase diagram showing the values of μ/t and Δ/t for which the topological phase occurs thermodynamically. Topological phase appears for the shaded regions, however it is absent for unshaded regions. The color coding of the shaded region represents the values of θ.
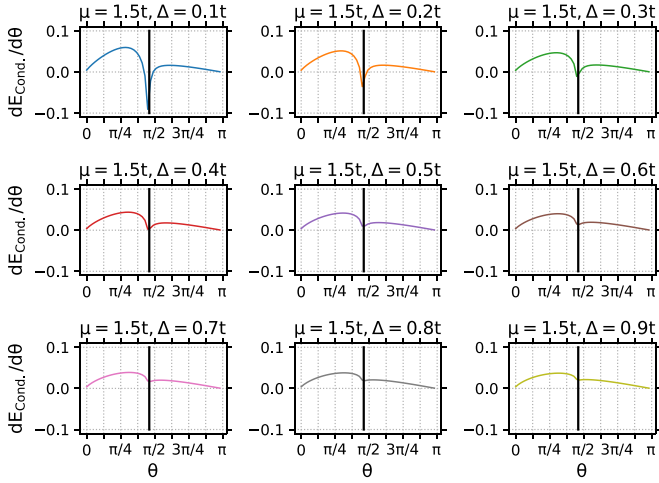
FIG. 12. Differentiation of condensation energy with respect to angle θ ($dE_{Cond.}/d\theta$) for $\mu = 1.5t$ and different Δ. The value of θ where ($dE_{Cond.}/d\theta$) = 0 local maximum or plateau occurs. The black vertical bar is the $\theta_{Topo.}$ for $\mu = 1.5t$.

into and out of the topological phase thermodynamically. Although previously proposed heterostructures [8] used the same broad idea, in this work no external magnetic field is needed to produce such an effect.

VII. PROPOSAL FOR EXPERIMENTAL HETEROSTRUCTURE

Usually tunneling experiments are employed to detect the Majorana fermions [17]. The proposed experimental setups for detecting Majorana fermions in strongly correlated wires are shown in Fig. 13. A zero bias peak in the conductance plot is usually interpreted as the possible signature of the MZM. However, these experiments are not at all conclusive, because Andreev bound states also have the same zero bias peak signature [61]. Despite these difficulties, recently a number of experiments have been performed to detect the MZM [8,10,62]. We propose analogous experiments to detect MZM.

In Fig. 13(a), a strongly correlated wire is placed on top of an insulating substrate. The tunneling electrons enters into the wire out through the metallic contacts. Furthermore, they exit the wire out through the superconducting contact and flow directly into the current measuring device. The chemical potential is controlled through the gate contacts. For nanowires, either heavy fermion [63–68] or transition metal [69–74] compounds can be used. Especially nanowires from transition-metal dichalcogenides compounds are promising candidates [71,73,74]. For superconductors one can use the iron-based materials, since they have an extended s-wave order parameter [32,45,75,76]. Because the spiral spin field is dynamically generated in strongly correlated 1D nanowires, we expect to see a MZM signature in the tunneling experiments, without the need of an external applied rotating magnetic field to generate spiral spin fields.

However, one can also perform experiments by externally inducing a noncollinear spin textures in the wire. The schematics for this corresponding experiment is shown in Fig. 13(b). Here, the only difference from the previous ar-
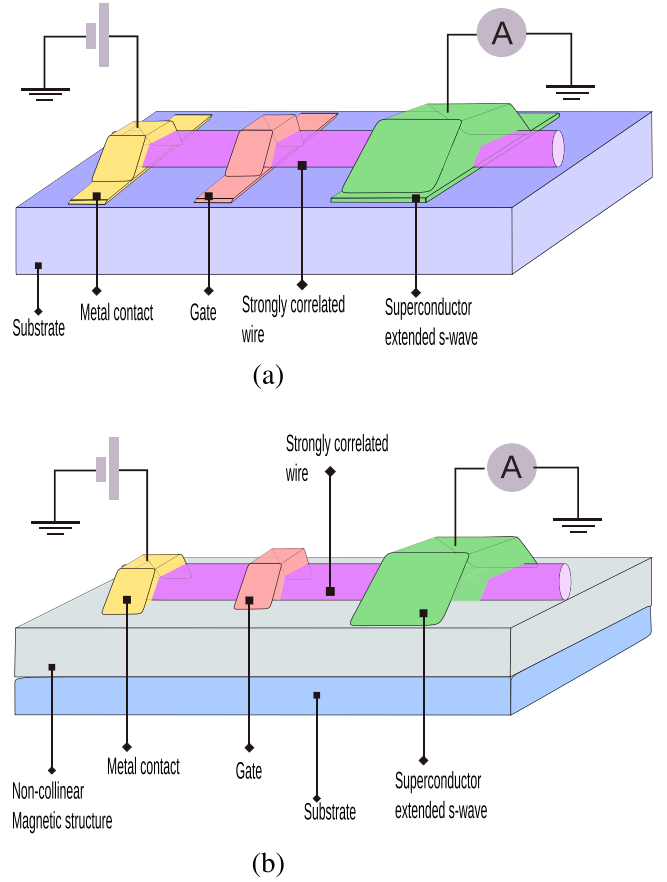
FIG. 13. Device schematics: (a) Tunneling experiment probing the presence of the Majorana fermions due to dynamic spin field of the 1D nanowire. (b) Tunneling experiment due to induced noncollinear spin texture through the bottom layer. One can use the Van der Waals magnets as the noncollinear magnetic layer.

rangement [Fig. 13(a)] is that we place the nanowire on a magnetic layer with noncollinear magnetic structures. The magnetic structure of the base magnetic material is induced into the nanowire, which is a necessary condition for the MZM to occur. One can also use the Van der Waals magnets as a magnetic layer [77,78]. They may host different magnetic structures, e.g., skyrmions, spirals [79–90], etc.

Finally, there is yet a third way to perform the required experiment. Instead of the nanowire, one can use a single wall carbon nanotube, which has the required strong correlation [91–93]. Interestingly, in these nanotubes RSOC can be induced and controlled through an electric field [94–96]. The schematic of the device is analogous to the one displayed in Fig. 13(a); instead of the nanowire, a single-wall carbon tube is placed over the metal contact, the gate, and the superconducting contact. One should remember in this case that the applied electric field also controls the RSOC.

The aforementioned experimental setup is known as local detection of MZM, however there also exist several nonlocal detections of the MZM [97]. In one of the schemes, basically one adds two extra gates to the two ends of the nanowires. The gate near the tunnel gate is denoted as the local gate, and the other is denoted as the nonlocal gate. The local gate measures the local density of states (dI/dV). When the nonlocal gate is

tuned, the MZM on the other side move towards the MZM at the local gate, and finally two MZMs merge with each other to create an interference pattern. It can be detected by the transformation of the dI/dV from the single peak at $V = 0$ to the double peak on two sides of $V = 0$. There also exist the three terminal circuits where two tunnel gates are placed at two sides of the superconducting induced wire. As these tunnel gate measures the local density of states on the two sides, one can use measure the dI/dV on the two sides of the wire. It the MZM is present at two ends of the nanowire, the zero bias peak corresponding to these two MZMs should be correlated. Apart from electric measurement, there also exist the caloric function measurement of the MZM [37,98].

For application of our model to real systems, the following energy scales of different parameters should be satisfied. If a is the lattice constant and m is the electric effective mass, then the hopping strength is $t = \hbar^2/ma^2$. We assume that the RSOC in the wire is comparable to the values in two-dimensional quantum wells having heavy elements; RSOC in these materials in the continuous limit is $\alpha_{\text{cont.}} \sim 10^4 - 10^5$ m/s. However, as we are considering the lattice model, instead of the continuous limit RSOC ($\alpha_{\text{cont.}}$) we need to use the lattice RSOC ($\alpha_{\text{Lat.}}$). The $\alpha_{\text{cont.}}$ is related to the lattice limit as $\alpha_{\text{Lat.}} = \frac{\hbar}{a}\alpha_{\text{cont.}}$. In a semiconductor with heavy elements, the electron effective mass is of order $m \sim 0.05m_e$. Putting all the values together, we will get $m\alpha_{\text{cont.}}^2 = \alpha_{\text{Lat.}}^2/t \sim 1$ K. For a reasonable proximity effect $\Delta \sim 1 - 10$ K. Hence the relevant hierarchy of energy will be $U \gg t > \alpha_{\text{Lat.}} > \Delta$. In the absence of RSOC, one can set $\alpha_{\text{Lat.}} = 0$.

We should make a small comment about the extended s-wave iron-based superconductors. One usually expects that the order parameter in this case will have nodes. This means the superconducting gap will close, which will destroy the topological phase. However, recent experimental works, although not fully convincing, have shown otherwise (see Sec. VIII of Ref. [99]). It was argued that spin-orbit coupling and interband pairing can give rise to the nodeless superconducting order parameter.

VIII. CONCLUSION

In this work, it was shown that the Majorana zero modes in nanowire-superconductor heterostructures can emerge without application of an external magnetic field; the only condition is that the electrons in the nanowire should be required to be strongly correlated. Within a mean-field treatment of Eq. (6) that ignores the no double occupancy constraint, the Hubbard operators are replaced with the conventional electron operators, $X^{\sigma 0} \rightarrow c_\sigma^\dagger$, $X^{0\sigma} \rightarrow c_\sigma$, $X^{00} \rightarrow \sum_\sigma c_\sigma^\dagger c_\sigma$, etc. As

a result, the Hamiltonian reduces to an exactly solvable one that produces the doubly degenerate band structure. To effectively generate the spinless fermions, one needs to separate the bands by adding into consideration a large external magnetic field. This, however, may totally destroy the superconductivity. To avoid such a scenario, we apply the mean-field treatment only after the no double occupancy constraint has been rigorously imposed. Within our approach, there is no electron double occupancy since the spinless fermion field $\xi_i^2 \equiv 0$. The spinless fermion excitations emerge in the absence of an external magnetic field. This is the reason we do not need z magnetic field when strong e-e correlation is present.

The physical system shown in Fig. 1 was investigated for a spiral spin field, both in the presence and absence of the Rashba spin-orbit coupling (RSOC). It was found that, apart from the chemical potential (μ), an extra parameter θ—the angle between spin projection of the neighboring sites on the xy plane—enters into the Hamiltonian as a tuning parameter for allowing the system to go into and out of the topological phase. This can be easily observed by comparing the single-mode energy as described by Eq. (21), with the same single-mode energy displayed by Kitaev's toy model [2,3]. The increase in θ decreases the allowed values of μ and t for which the system enters into the topological phase, as shown in Fig. 3. We investigated the θ dependence of the internal energy, and we found out that only for limited values of μ and Δ does the system thermodynamically enter into the topological phase, as shown in Figs. 9 and 10. The corresponding phase diagram is shown in Fig. 11. We also found out that RSOC is not a necessary ingredient for the appearance of the topological phase. This result is different from the usual semiconductor-superconductor heterostructure used for the realization of Majorana fermions, where RSOC, as well as an external magnetic field, are the necessary ingredients. In fact, in our case with an increase in intensity of RSOC, the area in the parameter phase space ($\mu/t - \theta$) for the occurrence of topological phase decreases, as shown in Fig. 8. Finally, in Sec. VII we proposed possible ways to experimentally realize the proposed system.

[1] S. D. Sarma, M. Freedman, and C. Nayak, Majorana zero modes and topological quantum computation, npj Quantum Inf. **1**, 15001 (2015).

[2] A. Y. Kitaev, Unpaired Majorana fermions in quantum wires, Phys. Usp. **44**, 131 (2001).

[3] J. Alicea, New directions in the pursuit of Majorana fermions in solid state systems, Rep. Prog. Phys. **75**, 076501 (2012).

[4] A. Manchon, H. C. Koo, J. Nitta, S. M. Frolov, and R. A. Duine, New perspectives for Rashba spin–orbit coupling, Nat. Mater. **14**, 871 (2015).

[5] K. Flensberg, F. Von Oppen, and A. Stern, Engineered platforms for topological superconductivity and Majorana zero modes, Nat. Rev. Mater. **6**, 944 (2021).

[6] M. Z. Hasan and C. L. Kane, Colloquium: Topological insulators, Rev. Mod. Phys. **82**, 3045 (2010).

[7] X.-L. Qi and S.-C. Zhang, Topological insulators and superconductors, Rev. Mod. Phys. **83**, 1057 (2011).

[8] R. M. Lutchyn, E. P. A. M. Bakkers, L. P. Kouwenhoven, P. Krogstrup, C. M. Marcus, and Y. Oreg, Majorana zero modes in superconductor–semiconductor heterostructures, Nat. Rev. Mater. **3**, 52 (2018).

[9] S. Nadj-Perge, I. K. Drozdov, B. A. Bernevig, and A. Yazdani, Proposal for realizing Majorana fermions in chains of magnetic atoms on a superconductor, Phys. Rev. B **88**, 020407 (2013).

[10] S. Nadj-Perge, I. K. Drozdov, J. Li, H. Chen, S. Jeon, J. Seo, A. H. MacDonald, B. A. Bernevig, and A. Yazdani, Observation of Majorana fermions in ferromagnetic atomic chains on a superconductor, Science **346**, 602 (2014).

[11] J.-P. Xu, M.-X. Wang, Z. L. Liu, J.-F. Ge, X. Yang, C. Liu, Z. A. Xu, D. Guan, C. L. Gao, D. Qian, Y. Liu, Q.-H. Wang, F.-C. Zhang, Q.-K. Xue, and J.-F. Jia, Experimental detection of a majorana mode in the core of a magnetic vortex inside a topological insulator-superconductor $Bi_2Te_3/NbSe_2$ heterostructure, Phys. Rev. Lett. **114**, 017001 (2015).

[12] R. M. Lutchyn, J. D. Sau, and S. Das Sarma, Majorana fermions and a topological phase transition in semiconductor-superconductor heterostructures, Phys. Rev. Lett. **105**, 077001 (2010).

[13] J. D. Sau, R. M. Lutchyn, S. Tewari, and S. Das Sarma, Robustness of Majorana fermions in proximity-induced superconductors, Phys. Rev. B **82**, 094522 (2010).

[14] H. Yu, N. F. Q. Yuan, W.-J. Li, L.-C. Chen, Z.-Y. Cao, D. Li, X. Qin, C.-D. Gong, and X.-J. Chen, Topological superconductivity in a topological insulator, arXiv:2208.09609 [cond-mat].

[15] L. Fu and C. L. Kane, Superconducting proximity effect and majorana fermions at the surface of a topological insulator, Phys. Rev. Lett. **100**, 096407 (2008).

[16] J. J. He, T. K. Ng, P. A. Lee, and K. T. Law, Selective equal-spin andreev reflections induced by majorana fermions, Phys. Rev. Lett. **112**, 037001 (2014).

[17] V. Mourik, K. Zuo, S. M. Frolov, S. R. Plissard, E. P. A. M. Bakkers, and L. P. Kouwenhoven, Signatures of majorana fermions in hybrid superconductor-semiconductor nanowire devices, Science **336**, 1003 (2012).

[18] T.-P. Choy, J. M. Edge, A. R. Akhmerov, and C. W. J. Beenakker, Majorana fermions emerging from magnetic nanoparticles on a superconductor without spin-orbit coupling, Phys. Rev. B **84**, 195442 (2011).

[19] B. Jäck, Y. Xie, J. Li, S. Jeon, B. A. Bernevig, and A. Yazdani, Observation of a Majorana zero mode in a topologically protected edge channel, Science **364**, 1255 (2019).

[20] Y. L. Chen, J. G. Analytis, J.-H. Chu, Z. K. Liu, S.-K. Mo, X. L. Qi, H. J. Zhang, D. H. Lu, X. Dai, Z. Fang, S. C. Zhang, I. R. Fisher, Z. Hussain, and Z.-X. Shen, Experimental realization of a three-dimensional topological insulator, Bi_2Te_3, Science **325**, 178 (2009).

[21] Y. Xia, D. Qian, D. Hsieh, L. Wray, A. Pal, H. Lin, A. Bansil, D. Grauer, Y. S. Hor, R. J. Cava, and M. Z. Hasan, Observation of a large-gap topological-insulator class with a single Dirac cone on the surface, Nat. Phys. **5**, 398 (2009).

[22] C. Chen, S. He, H. Weng, W. Zhang, L. Zhao, H. Liu, X. Jia, D. Mou, S. Liu, J. He, Y. Peng, Y. Feng, Z. Xie, G. Liu, X. Dong, J. Zhang, X. Wang, Q. Peng, Z. Wang, S. Zhang, F. Yang, C. Chen, Z. Xu, X. Dai, Z. Fang, and X. J. Zhou, Robustness of topological order and formation of quantum well states in topological insulators exposed to ambient environment, Proc. Natl. Acad. Sci. USA **109**, 3694 (2012).

[23] H. Kim, A. Palacio-Morales, T. Posske, L. Rózsa, K. Palotás, L. Szunyogh, M. Thorwart, and R. Wiesendanger, Toward tailoring Majorana bound states in artificially constructed magnetic atom chains on elemental superconductors, Sci. Adv. **4**, eaar5251 (2018).

[24] A. Kamlapure, L. Cornils, J. Wiebe, and R. Wiesendanger, Engineering the spin couplings in atomically crafted spin chains on an elemental superconductor, Nat. Commun. **9**, 3253 (2018).

[25] S. Ono, H. C. Po, and H. Watanabe, Refined symmetry indicators for topological superconductors in all space groups, Sci. Adv. **6**, eaaz8367 (2020).

[26] D. P. Arovas, E. Berg, S. A. Kivelson, and S. Raghu, The Hubbard model, Annu. Rev. Condens. Matter Phys. **13**, 239 (2022).

[27] M. Imada, A. Fujimori, and Y. Tokura, Metal-insulator transitions, Rev. Mod. Phys. **70**, 1039 (1998).

[28] S. B. Roy, *Mott Insulators: Physics and Applications*, IOP Expanding Physics (IOP, Bristol, 2019).

[29] P. B. Wiegmann, Superconductivity in strongly correlated electronic systems and confinement versus deconfinement phenomenon, Phys. Rev. Lett. **60**, 821 (1988).

[30] I. I. Mazin, Symmetry analysis of possible superconducting states in $K_xFe_ySe_2$ superconductors, Phys. Rev. B **84**, 024529 (2011).

[31] P. J. Hirschfeld, M. M. Korshunov, and I. I. Mazin, Gap symmetry and structure of Fe-based superconductors, Rep. Prog. Phys. **74**, 124508 (2011).

[32] G. R. Stewart, Superconductivity in iron compounds, Rev. Mod. Phys. **83**, 1589 (2011).

[33] F. Zhang, C. L. Kane, and E. J. Mele, Time-reversal-invariant topological superconductivity and majorana kramers pairs, Phys. Rev. Lett. **111**, 056402 (2013).

[34] H. Hosono, A. Yamamoto, H. Hiramatsu, and Y. Ma, Recent advances in iron-based superconductors toward applications, Mater. Today **21**, 278 (2018).

[35] T. Li, M. Burrello, and K. Flensberg, Coulomb-interaction-induced Majorana edge modes in nanowires, Phys. Rev. B **100**, 045305 (2019).

[36] P. Thalmeier and A. Akbari, Surface step states and Majorana end states in profiled topological-insulator thin films, Phys. Rev. B **104**, 184511 (2021).

[37] S. V. Aksenov, A. O. Zlotnikov, and M. S. Shustin, Strong Coulomb interactions in the problem of Majorana modes in a wire of the nontrivial topological class BDI, Phys. Rev. B **101**, 125431 (2020).

[38] E. M. Stoudenmire, J. Alicea, O. A. Starykh, and M. P. Fisher, Interaction effects in topological superconducting wires supporting Majorana fermions, Phys. Rev. B **84**, 014503 (2011).

[39] G. Bihlmayer, P. Noël, D. V. Vyalikh, E. V. Chulkov, and A. Manchon, Rashba-like physics in condensed matter, Nat. Rev. Phys. **4**, 642 (2022).

[40] M. Scheunert, W. Nahm, and V. Rittenberg, Graded lie algebras: generalization of hermitian representations, J. Math. Phys. **18**, 146 (1977).

[41] Due to induced superconducting gap Δ at the Fermi level of the wire the energy penalty for exciting a single electronic state from the top of the valence band to the bottom of the conduction

band in the wire is too high. It is due to our assumption $k_F^{SC} \gg k_F^{wire}$, which makes sure that $E_F^{wire} \sim \Delta$.

[42] F. W. J. Hekking and Yu. V. Nazarov, Subgap conductivity of a superconductor–normal-metal tunnel interface, Phys. Rev. B **49**, 6847 (1994).

[43] F. W. J. Hekking, L. I. Glazman, K. A. Matveev, and R. I. Shekhter, Coulomb blockade of two-electron tunneling, Phys. Rev. Lett. **70**, 4138 (1993).

[44] A pure spin-singlet s-wave pairing $\Delta_{i,i}^{\uparrow \downarrow}$ does not contribute to δH since it is multiplied by a corresponding bilinear form of the Hubbard operators that disappear at the coinciding lattice sites, e.g., $X_i^{\sigma 0} X_i^{\sigma' 0} = 0$. This is a direct manifestation of strong electron correlation that prohibits on-site double electron occupancy due to infinitely strong on-site Coulomb repulsion. In this case, the proximity-induced pairing is only possible provided the bulk superconductor develops either the spin-triplet p-wave pairing or an extended s-wave one. A pure s-wave pairing is totally excluded.

[45] G. R. Stewart, Unconventional superconductivity, Adv. Phys. **66**, 75 (2017).

[46] A. Ferraz and E. A. Kochetov, Effective action for strongly correlated electron systems, Nucl. Phys. B **853**, 710 (2011).

[47] E. A. Kochetov, SU(2) coherent-state path integral, J. Math. Phys. **36**, 4667 (1995).

[48] F. A. Berezin, Covariant and contravariant symbols of operators, Math. USSR-Izv. **6**, 1117 (1972).

[49] A. Ferraz and E. Kochetov, Fractionalization of strongly correlated electrons as a possible route to quantum Hall effect without magnetic field, Phys. Rev. B **105**, 245128 (2022).

[50] K. K. Kesharpu, E. A. Kochetov, and A. Ferraz, Topological Hall effect induced by classical large-spin background: $su(2)$ path-integral approach, Phys. Rev. B **107**, 155146 (2023).

[51] J. Herbrych, M. Šroda, G. Alvarez, M. Mierzejewski, and E. Dagotto, Interaction-induced topological phase transition and Majorana edge states in low-dimensional orbital-selective Mott insulators, Nat. Commun. **12**, 2955 (2021).

[52] Y. Oreg, G. Refael, and F. von Oppen, Helical liquids and majorana bound states in quantum wires, Phys. Rev. Lett. **105**, 177002 (2010).

[53] J. Li, H. Chen, I. K. Drozdov, A. Yazdani, B. A. Bernevig, and A. H. MacDonald, Topological superconductivity induced by ferromagnetic metal chains, Phys. Rev. B **90**, 235433 (2014).

[54] J. Klinovaja, P. Stano, A. Yazdani, and D. Loss, Topological superconductivity and majorana fermions in RKKY systems, Phys. Rev. Lett. **111**, 186805 (2013).

[55] B. Braunecker, G. I. Japaridze, J. Klinovaja, and D. Loss, Spin-selective Peierls transition in interacting one-dimensional conductors with spin-orbit interaction, Phys. Rev. B **82**, 045127 (2010).

[56] K. K. Kesharpu, Factors affecting the topological Hall effect in strongly correlated layered magnets: spin of the magnetic atoms, polar and azimuthal angle subtended by the spin texture, arXiv:2305.13423 [cond-mat].

[57] The Kitaev model is represented as

$$H^K = \sum_i -t f_i f_{i+1}^\dagger + \Delta f_i^\dagger f_{i+1}^\dagger + \text{H.c.} + \mu f_i f_i^\dagger.$$

It is also symmetric under time-reversal transformation.

[58] If $-2t \cos(\theta/2) \cos k < \mu < 0$, then, due to an unfilled band, the system behaves as metal. However, if $\mu \approx 0$ and the Fermi energy lies inside the band gap, and the system behaves as an insulator.

[59] A. Ferraz and E. Kochetov, Connection between the Kitaev chain and the Gutzwiller-projected BCS model, Ann. Phys. **456**, 169234 (2023).

[60] M. Tinkham, *Introduction to Superconductivity* (Courier, Mineola, New York, 2004).

[61] E. Prada, P. San-Jose, M. W. A. De Moor, A. Geresdi, E. J. H. Lee, J. Klinovaja, D. Loss, J. Nygård, R. Aguado, and L. P. Kouwenhoven, From Andreev to Majorana bound states in hybrid superconductor–semiconductor nanowires, Nat. Rev. Phys. **2**, 575 (2020).

[62] Z. Cao, S. Chen, G. Zhang, and D. E. Liu, Recent progress on Majorana in semiconductor-superconductor heterostructures—engineering and detection, Sci. China Phys. Mech. Astron. **66**, 267003 (2023).

[63] E. Morosan, D. Natelson, A. H. Nevidomskyy, and Q. Si, Strongly correlated materials, Adv. Mater. **24**, 4896 (2012).

[64] S. Paschen and Q. Si, Quantum phases driven by strong correlations, Nat. Rev. Phys. **3**, 9 (2021).

[65] M. H. Carvalho, G. S. Freitas, J. C. Souza, R. B. Campanelli, H. B. Pizzi, S. G. Mercena, M. Puydinger Dos Santos, F. Béron, P. F. S. Rosa, K. Pirota, and P. G. Pagliuso, Possible routes for the synthesis of nanowires of intermetallic compounds: The case of CeIn$_3$, J. Phys.: Conf. Ser. **2164**, 012041 (2022).

[66] K. O. Moura, L. a. S. de Oliveira, P. F. S. Rosa, C. B. R. Jesus, M. E. Saleta, E. Granado, F. Béron, P. G. Pagliuso, and K. R. Pirota, Dimensionality tuning of the electronic structure in Fe3Ga4 magnetic materials, Sci. Rep. **6**, 28364 (2016).

[67] P. F. S. Rosa, L. A. S. de Oliveira, C. B. R. de Jesus, K. O. Moura, C. Adriano, W. Iwamoto, T. M. Garitezi, E. Granado, M. E. Saleta, K. R. Pirota, and P. G. Pagliuso, Exploring the effects of dimensionality on the magnetic properties of intermetallic nanowires, Solid State Commun. **191**, 14 (2014).

[68] Z. Yang, H. Yang, L. Shang, and T. Zhang, Ordered PtFeIr intermetallic nanowires prepared through a silica-protection strategy for the oxygen reduction reaction, Angew. Chem., Int. Ed. **61**, e202113278 (2022).

[69] T. Nautiyal, T. H. Rho, and K. S. Kim, Nanowires for spintronics: A study of transition-metal elements of groups 8–10, Phys. Rev. B **69**, 193404 (2004).

[70] A. Delin and E. Tosatti, Magnetic phenomena in 5d transition metal nanowires, Phys. Rev. B **68**, 144434 (2003).

[71] H. E. Lim, Y. Nakanishi, Z. Liu, J. Pu, M. Maruyama, T. Endo, C. Ando, H. Shimizu, K. Yanagi, S. Okada, T. Takenobu, and Y. Miyata, Wafer-scale growth of one-dimensional transition-metal telluride nanowires, Nano Lett. **21**, 243 (2021).

[72] S. J. Luo, G. Y. Guo, and A. Laref, Magnetism of 3d-transition metal (Fe, Co, and Ni) nanowires on w-BN (0001), J. Phys. Chem. C **113**, 14615 (2009).

[73] H. E. Lim, Z. Liu, J. Kim, J. Pu, H. Shimizu, T. Endo, Y. Nakanishi, T. Takenobu, and Y. Miyata, Nanowire-to-nanoribbon conversion in transition-metal chalcogenides: Implications for one-dimensional electronics and optoelectronics, ACS Appl. Nano Mater. **5**, 1775 (2022).

[74] J. Li, K. Yao, Y. Huang, J. Fang, P. S. Kollipara, D. E. Fan, and Y. Zheng, Tunable strong coupling in transition metal dichalcogenide nanowires, Adv. Mater. **34**, 2200656 (2022).

[75] Y. Bang and G. R. Stewart, Superconducting properties of the $s^{\pm}$-wave state: Fe-based superconductors, J. Phys.: Condens. Matter **29**, 123003 (2017).

[76] G. Biswal and K. L. Mohanta, A recent review on iron-based superconductor, Proceedings of the International Conference on Nanomaterials for Energy, Environment and Sustainability (ICNEES-2019), Mater. Today **35**, 207 (2021).

[77] Q. H. Wang, A. Bedoya-Pinto, M. Blei, A. H. Dismukes, A. Hamo, S. Jenkins, M. Koperski, Y. Liu, Q.-C. Sun, E. J. Telford, H. H. Kim, M. Augustin, U. Vool, J.-X. Yin, L. H. Li, A. Falin, C. R. Dean, F. Casanova, R. F. L. Evans, M. Chshiev, A. Mishchenko, C. Petrovic, R. He, L. Zhao, A. W. Tsen, B. D. Gerardot, M. Brotons-Gisbert, Z. Guguchia, X. Roy, S. Tongay, Z. Wang, M. Z. Hasan, J. Wrachtrup, A. Yacoby, A. Fert, S. Parkin, K. S. Novoselov, P. Dai, L. Balicas, and E. J. G. Santos, The magnetic genome of two-dimensional van der waals materials, ACS Nano **16**, 6960 (2022).

[78] E. Elahi, G. Dastgeer, G. Nazir, S. Nisar, M. Bashir, H. Akhter Qureshi, D.-k. Kim, J. Aziz, M. Aslam, K. Hussain, M. A. Assiri, and M. Imran, A review on two-dimensional (2D) magnetic materials and their potential applications in spintronics and spin-caloritronic, Comput. Mater. Sci. **213**, 111670 (2022).

[79] J. Klein, T. Pham, J. D. Thomsen, J. B. Curtis, T. Denneulin, M. Lorke, M. Florian, A. Steinhoff, R. A. Wiscons, J. Luxa, Z. Sofer, F. Jahnke, P. Narang, and F. M. Ross, Control of structure and spin texture in the van der Waals layered magnet CrSBr, Nat. Commun. **13**, 5420 (2022).

[80] B. Yang, Y. Li, H. Xiang, H. Lin, and B. Huang, Moiré magnetic exchange interactions in twisted magnets, Nat. Comput. Sci. **3**, 314 (2023).

[81] M. J. Meijer, J. Lucassen, R. A. Duine, H. J. Swagten, B. Koopmans, R. Lavrijsen, and M. H. D. Guimarães, Chiral spin spirals at the surface of the van der waals ferromagnet Fe_3GeTe_2, Nano Lett. **20**, 8563 (2020).

[82] B. W. Casas, Y. Li, A. Moon, Y. Xin, C. McKeever, J. Macy, A. K. Petford-Long, C. M. Phatak, E. J. G. Santos, E. S. Choi, and L. Balicas, Coexistence of merons with skyrmions in the centrosymmetric van der waals ferromagnet $Fe_{5-x}GeTe_2$, Adv. Mater. **35**, 2212087 (2023).

[83] Y. Wu, B. Francisco, Z. Chen, W. Wang, Y. Zhang, C. Wan, X. Han, H. Chi, Y. Hou, A. Lodesani, G. Yin, K. Liu, Y.-t. Cui, K. L. Wang, and J. S. Moodera, A van der waals interface hosting two groups of magnetic skyrmions, Adv. Mater. **34**, 2110583 (2022).

[84] K. Hejazi, Z.-X. Luo, and L. Balents, Noncollinear phases in moiré magnets, Proc. Natl. Acad. Sci. USA **117**, 10721 (2020).

[85] C. Wang, Y. Gao, H. Lv, X. Xu, and D. Xiao, Stacking domain wall magnons in twisted van der waals magnets, Phys. Rev. Lett. **125**, 247201 (2020).

[86] Y. Wu, S. Zhang, J. Zhang, W. Wang, Y. L. Zhu, J. Hu, G. Yin, K. Wong, C. Fang, C. Wan, X. Han, Q. Shao, T. Taniguchi, K. Watanabe, J. Zang, Z. Mao, X. Zhang, and K. L. Wang, Néel-type skyrmion in WTe_2/Fe_3GeTe_2 van der Waals heterostructure, Nat. Commun. **11**, 3860 (2020).

[87] Q. Tong, M. Chen, and W. Yao, Magnetic proximity effect in a van der waals moire superlattice, Phys. Rev. Appl. **12**, 024031 (2019).

[88] M. Yang, Q. Li, R. V. Chopdekar, R. Dhall, J. Turner, J. D. Carlström, C. Ophus, C. Klewe, P. Shafer, A. T. N'Diaye, J. W. Choi, G. Chen, Y. Z. Wu, C. Hwang, F. Wang, and Z. Q. Qiu, Creation of skyrmions in van der Waals ferromagnet Fe_3GeTe_2 on (Co/Pd)$_n$ superlattice, Sci. Adv. **6**, eabb5157 (2020).

[89] Q. Tong, F. Liu, J. Xiao, and W. Yao, Skyrmions in the Moiré of van der Waals 2D Magnets, Nano Lett. **18**, 7194 (2018).

[90] K. S. Burch, D. Mandrus, and J.-G. Park, Magnetism in two-dimensional van der Waals materials, Nature (London) **563**, 47 (2018).

[91] W. Izumida, K. Sato, and R. Saito, Spin–orbit interaction in single wall carbon nanotubes: symmetry adapted tight-binding calculation and effective model analysis, J. Phys. Soc. Jpn. **78**, 074707 (2009).

[92] J.-S. Jeong and H.-W. Lee, Curvature-enhanced spin-orbit coupling in a carbon nanotube, Phys. Rev. B **80**, 075409 (2009).

[93] *Single-Walled Carbon Nanotubes: Preparation, Properties and Applications*, edited by Y. Li and S. Maruyama, Topics in Current Chemistry Collections (Springer International, Cham, 2019).

[94] H. Min, J. E. Hill, N. A. Sinitsyn, B. R. Sahu, L. Kleinman, and A. H. MacDonald, Intrinsic and Rashba spin-orbit interactions in graphene sheets, Phys. Rev. B **74**, 165310 (2006).

[95] J. Klinovaja, M. J. Schmidt, B. Braunecker, and D. Loss, Helical modes in carbon nanotubes generated by strong electric fields, Phys. Rev. Lett. **106**, 156809 (2011).

[96] D. S. Novikov and L. S. Levitov, Energy anomaly and polarizability of carbon nanotubes, Phys. Rev. Lett. **96**, 036402 (2006).

[97] H. Zhang, D. E. Liu, M. Wimmer, and L. P. Kouwenhoven, Next steps of quantum transport in Majorana nanowire devices, Nat. Commun. **10**, 5128 (2019).

[98] M. S. Shustin and S. V. Aksenov, Features of physical observables of a strongly correlated superconducting nanowire with rashba spin–orbit interaction, J. Exp. Theor. Phys. **135**, 500 (2022).

[99] S. Qin, C. Fang, F.-C. Zhang, and J. Hu, Topological superconductivity in an extended s-wave superconductor and its implication to iron-based superconductors, Phys. Rev. X **12**, 011030 (2022).